








Transition Region from Turbulent to Dead Zone in Protoplanetary Disks: Local Shearing Box Simulations

Fulvia Pucci^{1,2} , Kengo Tomida⁴ , James Stone³ , Shinsuke Takasao⁵ , Hantao Ji² , and Shoichi Okamura^{1,6}

¹ International Research Collaboration Center, National Institutes of Natural Sciences, Tokyo 105-0001, Japan; pucci@nins.jp, fpucci@princeton.edu

² Princeton University, Astrophysics Department, Princeton, NJ, USA; hji@pppl.gov

³ The Institute for Advanced Study, 1 Einstein Drive, Princeton, NJ 08540, USA; jmstone@ias.edu

⁴ Astronomical Institute, Tohoku University, Sendai, Miyagi 980-8578, Japan; tomida@astr.tohoku.ac.jp

⁵ Department of Earth and Space Science, Osaka University, Toyonaka, Osaka 560-0043, Japan; takasao@astro-osaka.jp

⁶ National Institute for Fusion Science, National Institutes of Natural Sciences, Toki 509-5292, Japan; okamura@nifs.ac.jp

Received 2020 August 12; revised 2020 November 8; accepted 2020 November 10; published 2021 January 20

Abstract

The dynamical evolution of protoplanetary disks is of key interest for building a comprehensive theory of planet formation and to explain the observational properties of these objects. Using the magnetohydrodynamics code Athena++, with an isothermal shearing box setup, we study the boundary between the active and dead zone, where the accretion rate changes and mass can accumulate. We quantify how the turbulence level is affected by the presence of a non-uniform Ohmic resistivity in the radial x direction that leads to a region of inhibited turbulence (or dead zone). Comparing the turbulent activity to that of ideal simulations, the turbulence-inhibited area shows density fluctuations and magnetic activity at its boundaries, driven by energy injection from the active (ideal) zone boundaries. We find magnetic dissipation to be significantly stronger in the ideal regions, and the turbulence penetration through the boundary of the dead zone is determined by the value of the resistivity itself, through the Ohmic dissipation process, though the thickness of the transition does not play a significant role in changing the dissipation. We investigate the 1D spectra along the shearing direction: magnetic spectra appear flat at large scales both in ideal as well as resistive simulations, though a Kolmogorov scaling over more than one decade persists in the dead zone, suggesting the turbulent cascade is determined by the hydrodynamics of the system: magnetorotational instability dynamo action is inhibited where sufficiently high resistivity is present.

Unified Astronomy Thesaurus concepts: [Star formation \(1569\)](#); [Stellar accretion disks \(1579\)](#); [Planet formation \(1241\)](#)

1. Introduction

To fully understand planet formation, a global picture of protoplanetary disk (PPD) evolution is required, which implies understanding the interaction of magnetic field with partially ionized gases, or plasmas, often with significant amounts of dust. Magnetohydrodynamics (MHD) allows the exploration of the planetary formation environment, turbulent angular momentum transport, interactions with the disk, and orbital migration.

One of the main difficulties in understanding PPD dynamics lies in the mechanism(s) allowing accretion of material onto the star, which must remove angular momentum of the accreting material itself in orbital quasi-equilibrium, allowing flows into the inner regions of the disk, shaping the disk structure, as has been observed by ALMA. Possible sources of angular momentum transport are magneto-centrifugally driven winds (e.g., Blandford & Payne 1982), and the effective viscous stresses introduced by the magnetorotational instability (MRI; Hawley & Balbus 1995), whose nonlinear outcome in the ideal MHD limit is the development of MHD turbulence. Self-gravity in conjunction with differential rotation has also been examined as a mechanism for driving turbulence by Wada & Norman (1999, 2007) as well as the effect of hydrodynamical instabilities (Zeldovich 1981). Placing this model in the context of global disk structure and its interaction with the central star makes the problem very challenging, involving a wide range of temporal and spatial scales, coupled via nonlinear dynamical processes.

Accurately capturing the full non-ideal physics is computationally difficult, and numerical expense limits the feasible resolution and/or run length, so global simulations but also local shearing

box simulations have been carried out to study the saturation of the MRI (Balbus & Hawley 2003). Key aspects only addressed by global models are the actual transport of angular momentum, the wind launching, the feedback of magnetic fields on disk structure, and the long-term evolution of the disk. One of the important findings by local MHD simulations is that the net vertical magnetic field controls the saturation level of the turbulence (Hawley et al. 1995; Sano et al. 2004; Pessah et al. 2007; Suzuki & Inutsuka 2009; Okuzumi & Hirose 2011; Simon et al. 2013, 2018), which essentially determines the strength of the transport of angular momentum and resulting mass accretion (Suzuki & Inutsuka 2014). In the shearing box the accretion is not actually simulated because of the symmetries that characterize the setup, while the shearing motion generates the effective viscosity (helping the angular momentum transport) through the MRI instability, so that the accretion rate is simply estimated from the stress tensor under the time-steady condition. Except for the innermost regions of PPDs, where the temperature $T \sim 1000$ K, and the disk surface layers ionized by sources such as stellar X-rays, FUV photons, and galactic cosmic rays, non-ideal MHD effects due to the low ionization levels of the gas (e.g., Blaes 1994; Sano et al. 2000) are expected to be important. These processes are dominant across most radii in PPDs (Armitage 2011; Turner et al. 2014). Gammie (1996) proposed what has now become the traditional dead-zone model in which disk surface layers accrete by sustaining MRI turbulence, with the shielded interior maintaining an inert and magnetically decoupled dead zone. Here, MRI turbulence is quenched by competing non-ideal MHD terms, depending on density, temperature, degree of magnetization, grain distribution,

and ionization (Balbus & Terquem 2001; Kunz & Balbus 2004; Desch & Turner 2015), i.e., in the location within the disk.

In disk regions between 1 and 5 au, Ohmic resistivity will be dominant near the mid-plane, the Hall effect at intermediate disk heights (intermediate densities; Wardle 2007), and ambipolar diffusion (AD) in low-density regions, higher up in the disk (e.g., Desch 2004). Though such non-ideal effects have long been recognized (e.g., Sano & Stone 2002a, 2002b) and studied using an analytical approach (Wardle 1999), it is only recently that shearing box simulations including AD and the Hall term have begun to be performed in the relevant parameter regimes with significant resolutions, leading to a modified picture of how disks accrete that deviates significantly from the traditional dead zone (e.g., Sano et al. 2000; Ilgner & Nelson 2006; Wardle & Salmeron 2012).

Lesur et al. (2014) included all three non-ideal MHD effects, and found that if $\Omega \cdot \mathbf{B} > 0$, the Hall effect can produce an azimuthal magnetic field and thus a large-scale Maxwell stress throughout the midplane of the disk. This result not only makes the disk more active in terms of accretion but can also increase the vertical scale height of the disk. Bai (2014) showed such an amplification of the horizontal field at the midplane drives stronger winds and enhances the wind-driven accretion up to 50%. Simon et al. (2015) remarked that the Hall effect is important even to qualitatively understand the disk structure and the accretion process and found bursty accretion events, possible due to Hall-mediated whistler unstable modes in the disk. The role of non-ideal effects has also been studied in the context of global simulations (Gressel et al. 2015; Béthune et al. 2017), in comparison with shearing box models (Bai & Stone 2013), showing the wind solution arises naturally in global simulations.

Before building a comprehensive model of global accretion disks it is necessary to understand the basic local properties of the plasma in which planet formation is embedded. Fleming & Stone (2003) studied, within a local shearing box setup, the evolution of MRI in vertically stratified accretion disks, i.e., with the ionization degree depending on height. They found the disk to remain quiescent in the central resistive region of the domain, while Reynolds stresses remain above 10% the Maxwell stresses in the active layer, producing a significant contribution to the effective viscosity, α . They suggested a residual mass inflow in the resistive layers from the active zone. Okuzumi & Hirose (2011) found that the vertical structure is mainly affected by the vertical magnetic flux and the critical heights, the latter defining the atmosphere, the active, and the dead zone, and it is insensitive to the details of the resistivity profile.

Even simulations that are supposedly carried out within ideal MHD are actually affected by some form of numerical resistivity.

Sano et al. (1998), assuming an initial weak uniform magnetic field in the vertical direction, introduced a definition of the effective⁷ magnetic Reynolds number $\bar{R}_m = v_A^2 / (\eta \Omega)$, where v_A is the Alfvén speed, η is the magnetic diffusivity, and Ω the angular velocity. They obtained this magnetic Reynolds number $R_m = v_A L / \eta$ assuming $L = v_A / \Omega$, i.e., the characteristic MRI length scale. This allowed them to study the turbulence behavior in the nonlinear stage. They found that when $\bar{R}_m \geq 1$, the MRI does not saturate and channel flows develop in the system (see also Sano & Stone 2002a, 2002b).

In the case of a poloidal field with zero vertical net flux, Fleming et al. (2000) argued that the MRI can be sustained when the effective magnetic Reynolds number $\bar{R}_m := c_s^2 / \eta \Omega \geq 10^4$. Note the same relation can be written in terms of the Alfvén speed v_A , once the relation between the Alfvén and sound speed is established. They also defined a Reynolds number below which, in a numerical simulation with a typical vertical scale H and box size of length L , the computational box will be dominated by diffusion on a timescale Ω . They found this minimum Reynolds number to be $R_m^{\text{cr}} \sim (2\pi/L)(Hc_s/\Omega)$.

Nauman & Blackman (2017) defined a Reynolds number $R_m = L_x^2 \Omega / \eta$, where the macroscopic length scale L_x is the size of the domain in the x direction. They found a threshold value for the magnetic Reynolds number of $R_m^{\text{th}} \sim 1000$ for which the magnetic turbulence can be sustained. They also found that these results are relevant for establishing the numerical resistivity values that can guarantee the convergence of the MRI-generated energy (kinetic and magnetic). We will discuss these concepts in the context of our own simulations in subsequent sections. In this paper we investigate the basic properties of the local MHD turbulence set by the MRI in a shearing box setup, where the resistivity profile changes in the x direction (radial direction in a global setup).

Unlike Okuzumi & Hirose (2011) we will consider a vertically uniform disk, and we will address the effect of a vertical stratification in a future paper. Note that in the presence of a shear viscosity, with a vertical stratification, a meridional circulation pattern sets in within the poloidal plane of the disk because of the vertical gradient of the radial velocity (Urpin 1984). This results in a 3D transport within the disk height. In our case the disk is threaded with a vertical magnetic field with nonzero net flux and we are interested in the radial transition region (x direction in our simulations) between a resistive and an ideal zone. The goal of the paper is to understand the properties of MRI in such a region, which is considered of paramount importance for planetesimal formation. The paper is organized as follows: in Section 2 we discuss the shearing box concept and setup. In Section 3 we study the turbulence development and the effective viscosity in an ideal shearing box setup. We discuss the momentum equation balance and the spectral features of the MRI-driven turbulence. In Section 4 we discuss the 1D spectral features in the shear direction, averaging in the vertical direction. In Section 5 we investigate the turbulence development in a setup where the magnetic resistivity depends on the x direction, with an ideal region and an area where the resistivity plays a role. In this context we study the origin of density accumulation and perturbations to the shear velocity at the transition between the resistive region and the ideal one. We discuss the spectral features of the transition region, comparing with the ideal simulation spectra. We summarize our results in the conclusions.

2. Setup for Shearing Box Simulations

The local shearing box approximation (Stone & Gardiner 2010) adopts a frame of reference located at a radius r_0 , corotating with the disk at orbital frequency $\Omega_0 = \Omega(r_0)$. In this frame, the equations of resistive MHD are written in a Cartesian coordinate system (x, y, z):

$$\partial_t \rho + \nabla \cdot (\rho \mathbf{v}) = 0 \quad (1)$$

⁷ By “effective” we mean based on small-scale turbulent fluctuations.

$$\begin{aligned} \partial_t(\rho\mathbf{v}) + \nabla \cdot (\rho\mathbf{v}\mathbf{v} + \mathcal{T}) \\ = \rho\Omega_0^2(2q\hat{x}\hat{i} - z\hat{k}) - 2\Omega_0\hat{k} \times (\rho\mathbf{v}) \end{aligned} \quad (2)$$

$$\partial_t\mathbf{B} = \nabla \times (\mathbf{v} \times \mathbf{B}) - \nabla \times (\eta\nabla \times \mathbf{B}) \quad (3)$$

where \hat{i} , \hat{j} and \hat{k} are the unit vectors defining the orthonormal triad, and we assume the magnetic permeability to be unity. We also adopt an isothermal equation of state $P = \rho c_s^2$ and set $c_s = 1$. The total stress tensor \mathcal{T} is defined as

$$\mathcal{T} = (P + B^2/2)I - \mathbf{B}\mathbf{B}, \quad (4)$$

where P is the gas pressure and I is the unite tensor⁸.

An equilibrium solution for the set of Equations (1)–(3) is $\mathbf{v}_0 = -q\Omega_0 x \hat{j}$, where the shear parameter q is defined as

$$q = -\frac{1}{2} \frac{d \ln \Omega^2}{d \ln r}, \quad (5)$$

i.e., for a Keplerian flow $q = 3/2$. The total velocity field is the equilibrium solution of the MHD equations plus a perturbation, $\mathbf{v} = \mathbf{v}_0 + \delta\mathbf{v}$.

The magnetic diffusivity η depends in general on the location, and in particular in our model the profile $\eta(x)$ is described in Section 5. We also assume the disk is threaded by a constant, uniform vertical magnetic field $\mathbf{B} = B_{0z}\hat{k} = \sqrt{\frac{P_0}{2\beta_0}}\hat{k}$, where β_0 is the plasma parameter at $t = 0$, $P_0 = \rho_0$ thanks to the isothermal equation of state, where ρ_0 is the initial uniform density, so $\rho_0 = 1$. Since our box has no vertical stratification, the magnetic field is not wound by the vertical differential rotation: the temperature being uniform, $\Omega = \Omega(x)$ does not depend on the vertical scale (generalization of the Von Zeipel theorem).

For our numerical calculations, we use the Athena++ code (Stone et al. 2020), a complete rewrite in C++ of the Athena code that integrates the shearing-box equations (1)–(3) using a standard Godunov scheme with second-order-accurate spatial reconstruction.

3. Comparing Ideal Shearing Box Simulations

In this section we discuss the turbulence development and force balance for ideal simulations described in Table 1, labeled as ID. We will then compare the latter with resistive setups (see Table 1, labeled as RES), to understand the effect of the size of the active zone. For ideal simulations different runs have the same number of cells and physical parameters, but they differ in size. This corresponds to having different wavevectors ($k \sim 2\pi n/L_z$, $n = (1,2,3\dots 512)$) available for instabilities to grow. Still, the ratio between the Alfvén and sound speed with the maximum available shear decreases with larger boxes.

Our fiducial model, labeled as IDB in Table 1, has $L_x = 8$, $L_y = 8$, $L_z = 1$, since, as we will show later, this allows enough space to discuss the nonuniform density accumulation in the resistive setups. For all of the simulations we resolve the critical length scale of the MRI, $\lambda_C = 9.18\beta^{-1/2} \sim 0.092$ (Hawley et al. 1995), and the maximum unstable wavelength of the MRI is $\lambda_{\max} \simeq 2\pi v_A/\Omega_0 \sim 0.3$ (for $\beta = 10^4$, see, e.g., Suzuki et al. 2010), where all the length scales are normalized to the scale height.

⁸ For the sake of clarity, we will use the capital letter B or \mathbf{B} to indicate the total magnetic field, and the lowercase b or \mathbf{b} to indicate the fluctuations. In the case where there is no background field, e.g., in the x direction, $B_x \equiv b_x$.

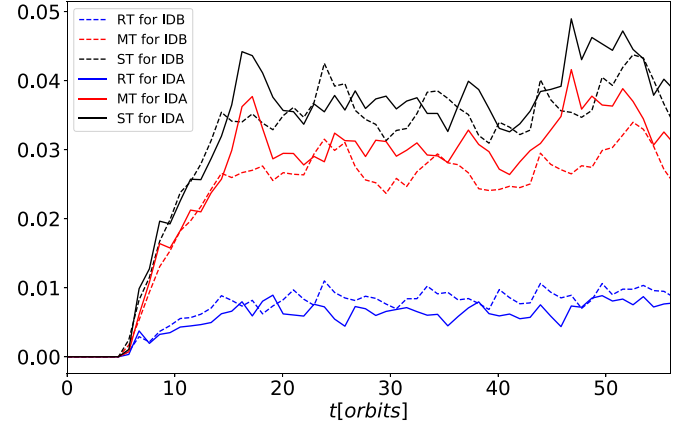


Figure 1. Reynolds (RT, blue), Maxwell (MT, red) and stress (ST, black) tensors for IDA (solid lines) and IDB (dashed lines), normalized to the pressure P . The saturation level for the stress tensor is around 0.035 for both simulations.

Table 1
Simulation Parameters

Name	N_x	N_y	N_z	η_0	β	L_x	L_y	L_z	a
IDA	512	512	64	0	10^4	4	4	1	N/A
IDB	512	512	64	0	10^4	8	8	1	N/A
RESA	512	512	64	10^{-1}	10^4	8	8	1	0.1
RESB	512	512	64	10^{-2}	10^4	8	8	1	0.1
RESC	512	512	64	10^{-2}	10^4	8	8	1	0.01

Note. N is The number of gridpoints in each direction, η_0 is the resistivity, β is the plasma parameter, L is the simulation size in each direction (in unit of the vertical scale), and a is the thickness of the transition between the resistive and the ideal zone, which does not apply (N/A) in ideal simulations.

3.1. MRI Development in Ideal MHD Shearing Box Simulations

We quantify the efficiency of the turbulence through the x - y component of the total stress tensor

$$T_{xy} = M_{xy} + R_{xy}, \quad (6)$$

where B_i and v_i ($i = x, y$) are the component of the magnetic and velocity fields respectively, $M_{xy} = \langle -B_x B_y \rangle$ is the Maxwell tensor and $R_{xy} = \langle \rho v_x \delta v_y \rangle$ is the Reynolds tensor; the brackets indicate the average over the y, z (vertical) direction. In Figure 1 we show for simulation IDA (solid lines) the effective viscosity $\alpha = \langle T_{xy} \rangle / \langle P(t) \rangle$, where the average is over the whole volume, i.e., the stress tensor normalized with the average pressure $\langle P(t) \rangle$; we also show the breakdown in the Reynolds and Maxwell tensors, also normalized with $\langle P(t) \rangle$. The saturation level of the stress tensor is about 0.035 in the case of a box characterized by a resolution of 64 grid points in the vertical direction, which is compatible with previous literature (e.g., Hawley et al. 1995, 1996; for a more recent simulation see, e.g., Shi et al. 2016). As expected, the main contribution to effective viscosity α is due to the Maxwell tensor.

For simulation IDB, we expect to have convergence of the stress tensor to the same value, since the resolution in the vertical direction (shown to be a key feature for convergence by Hawley et al. 1995) is the same. Indeed this is what we observe in Figure 1 (dashed lines), where the relative contributions

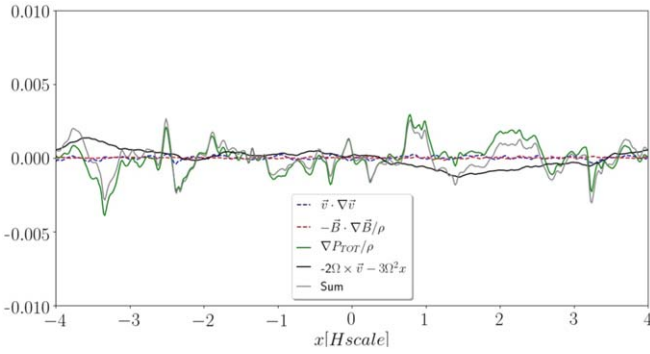


Figure 2. Contribution of each term in the x direction (radial) of Equation (2), i.e., the force balance for IDB. The fictitious forces balance each other and the residual difference between the Coriolis and the centrifugal force balances the fluctuations of the other terms. Each term is normalized to the the maximum of the centrifugal force.

of the Maxwell and Reynolds tensors for IDA and IDB are similar.

3.2. Numerical Resistivity for “Ideal Simulations”

Even if there is no explicit resistivity, we can estimate a magnetic diffusivity $\eta_N = v_A \Delta x = 0.0002$, where in our simulations $\Delta x = 1/64 = 0.0156$. The macroscopic Reynolds number $R = v_A L/\eta = 64$, where v_A is the Alfvén speed based on the initial vertical magnetic field and $L = 1$ is the size of the box (in units of the vertical scale). The (numerical) magnetic Prandtl number, since the numerical diffusivity and viscosity are calculated in the same way, is of order 1. We expect the MRI to develop in regions where the macroscopic Reynolds number $R_m > 1$.

In comparison with the other definition of the critical Reynolds number (see the introduction), we obtained $R_m = L_x^2 \Omega/\eta = 32 \times 10^4$ for the parameter defined in Nauman & Blackman (2017), which confirms magnetic turbulence should be sustained. Considering a similar definition by Fleming et al. (2000), our $\bar{R}_m \sim 10^4$, which is the threshold value for the turbulence to be sustained. In terms of the nonlinear evolution of the turbulence, using the parameter defined by Sano et al. (1998), we get $\bar{R}_m = v_A^2/\eta\Omega < 1$, i.e., we do not expect channel flows to dominate the simulation.

3.3. Force Balance for the Saturated Stationary State

As discussed in Section 2 a shearing box in a corotating frame with the disk includes the Coriolis and centrifugal terms in the momentum equation, see Equation (2). In Figure 2 we show the contribution of each term in Equation (2) for our fiducial model IDB. We can see the total pressure gradient fluctuations are balanced by a perturbation of the total fictitious forces. The pressure gradient modification (or equivalently the density gradient, given our isothermal ansatz) generated by the changes in the Coriolis force, reflects the compressibility of the system. The fluctuations in the pressure gradient are evident at all scales, mainly reflecting the spatial fluctuations of the hydrodynamic pressure.

4. Spectral Features of MHD Turbulence

One of the goals of this study is to understand the physics at the transition between the ideal MHD and strongly resistive MHD domains. We begin by discussing 1D spectra in the azimuthal plane for the ideal shearing box simulations. As we are looking for

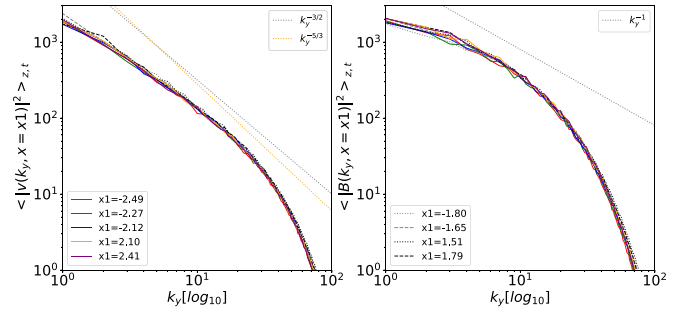


Figure 3. Kinetic (left) and magnetic (right) energy 1D spectra, defined in Equation (7), for simulation IDB. The spectra are averaged in the vertical direction (z) and over 20 orbital times, between orbit 40 and 60. Color labels the location x_1 at which the 1D Fourier transform has been calculated. For a better visualization the legend is spread among the two panels and refers to both of them. The velocity spectral slope is closer to $-3/2$, compared to the yellow dashed line indicating the Kolmogorov slope $-5/3$.

structures in the x - y plane (assuming the vertical direction is uniform), we will calculate the 1D Fourier transform along the y direction, for a selected position x_1 . We will then calculate the power spectrum averaged over the vertical direction (z direction). Finally we average over about 20 orbital times, once the MRI is saturated, to obtain the plotted quantity. In the formulae, for any field component $A_i(x, y, z, t)$, defining averages $\langle \rangle_x$ in terms of the subscript-independent variable x , we have

$$\langle |A_i(x_1, k_y)|^2 \rangle_{z,t} = \quad (7)$$

$$\left\langle \left| \int A_i(x_1, y, t) e^{-ik_y y} dy \right|^2 \right\rangle_{z,t} \quad (8)$$

$$k_y = 2\pi n/L_y \quad (9)$$

with $n = (1, 2, 3 \dots 512)$.

4.1. Ideal MHD Spectra

The result for the velocity field (rms) is plotted in Figure 3 (left), for the ideal simulation IDB, where colors label different values of x_1 . Figure 3 (left) shows that a power law can be identified in the kinetic energy spectrum. Fitting the points between $k_y = 2$ and $k_y = 20$ the velocity field spectral slope is close to $-3/2$. We also plot the $-5/3$ slope as reference.

Figure 3 (right) shows the magnetic energy spectrum at MRI saturation, where a power law is much harder to identify. In addition, the MRI-generated turbulence is not strongly magnetized, and the plasma β is very large. Intriguingly, solar wind turbulence, at a plasma $\beta \sim 1$, also shows velocity field spectral slopes close to $-3/2$, flatter than magnetic field spectra (see Bruno & Carbone 2013) in the inertial range, but steeper than magnetic energy spectra at the largest scales, where the power law in the solar wind is closer to k^{-1} . Our magnetic spectra have energies comparable to the velocity field at large scale, where the magnetic spectrum also appears to be relatively flat. However, the power law is visible for less than one decade, and it seems clear that injection is dominating at large scales. The spectra fall off at values close to $n \sim 70$, consistent with the magnetic Reynolds numbers estimate given above. We remark that larger magnetic Reynolds numbers should allow more extended inertial range and, according to the results in Nauman & Blackman (2017), to better resolve the turbulence, finding higher saturation values.

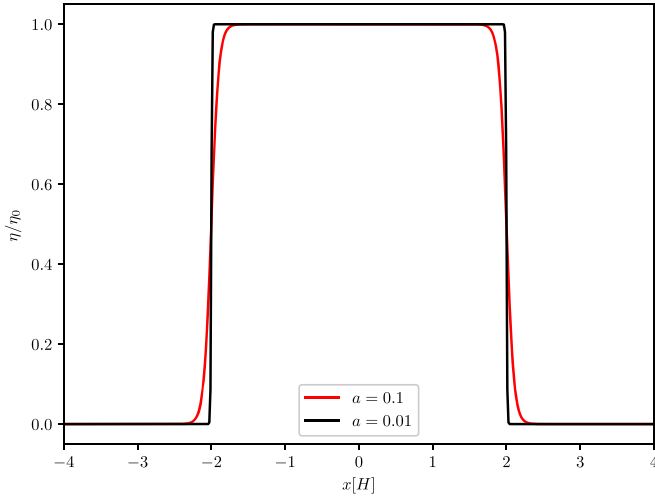


Figure 4. Resistivity profile as a function of the x coordinate for $x_0 = 1$ and $a = 0.1$ (red) and $a = 0.01$ (black).

5. MRI Development in Shearing Box Simulations with a Nonuniform Resistivity Profile

For resistive simulations the Ohmic resistivity profile is shown in Figure 4 and described by

$$\eta(x) = \frac{\eta_0}{2} (\tanh((x + x_0)/a) - \tanh((x - x_0)/a)), \quad (10)$$

where $x_0 = 2$.

The set of simulations we performed are described in Table 1 and labeled as RES, RESA and RESB differ in the value of the resistivity η_0 , while in RESC the parameters are the same as in RESB but the transition region is 10 times thinner. In RESB the transition is resolved by six grid points while in RESA the transition is not resolved.

Using for example the explicit resistivity for RESB, we can estimate the macroscopic Reynolds number $R = v_A L/\eta = 0.71 < 1$, so we expect the MRI to be inhibited in the regions where the macroscopic Reynolds number $R_m < 1$.

The MRI modes should then be quenched so it is worth comparing with the definition in Fleming et al. (2000) of a Reynolds number $R_m^{\text{cr}} \sim (2\pi/L)(Hc_s/\Omega)$, below which the computational box will be dominated by diffusion on timescale Ω . In our simulation $R_m^{\text{cr}} = 0.63$ so in the dead zone $R_m \sim R_m^{\text{cr}}$, i.e., based on this criterion all the MRI modes are damped. Note this is even more relevant for RESA for which the explicit resistivity is higher.

In Figure 5 (a) we show an example of how the density and magnetic field look in our simulation RESC after ~ 20 orbital times, when density seems to accumulate in the central resistive region (see the discussion in Section 5.4). A turbulent magnetic field develops in the x and y direction in the active zone, while in the resistive zone the magnetic turbulence is quenched. Oblique density fluctuations in the y - z plane are present; see Figure 5(b).

5.1. Stress Tensor in a Nonuniform Resistivity Setup

Our goal is to compare the structure and distribution of the turbulence in the active and dead zones with particular interest in the boundary between the dead and active regions. Since, as shown in Figure 1, the main contribution to the effective viscosity α is due to the magnetic tensor, we expect to see a significant variation in the case of a resistive domain. In

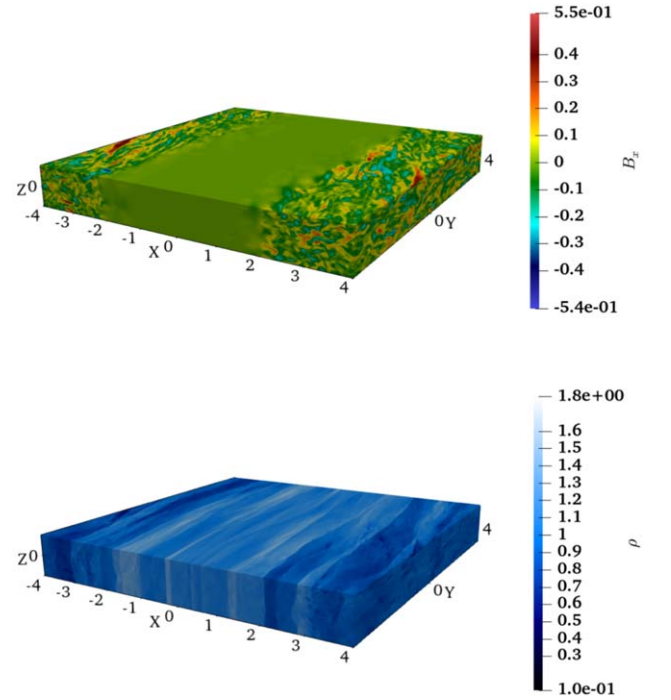


Figure 5. 3D profiles in simulation RESB after ~ 20 orbital times for (top) the x component of the magnetic field, where we see the field is developed in the ideal region of the domain and the transition to the inactive area is not sharp. (Bottom) Density profile ρ . Density fluctuations are oblique in the x - y plane.

Figure 6, for our fiducial simulation RESB, we show the (top) Reynolds tensor, (center) Maxwell tensor, normalized to the pressure P , and how they contribute to the total (bottom) α (stress tensor normalized with pressure P) averaged in the z and y direction, as defined in Equation (6) and described in Section 3.1. Each panel shows an average of the ideal regions (green) and the resistive central region (red).

For the first 50 orbits the stresses in the ideal region are quite similar (in terms of saturation levels and trends) to our fiducial model, simulation IDB (Figure 6), even if the actual saturation level in RESB is slightly less than 0.03. This lower value with respect to the ideal case is due to the lack of activity in the resistive region, which is suppressed by a relatively high resistivity. Indeed, we report for RESA, for which the resistivity is even higher $\eta_0 = 0.1$, a saturation level of 0.01.

Between $t \sim 20$ and $t \sim 50$ it seems the MRI reaches a saturated state. After $t \sim 50$ orbits, very high fluctuations in the stress tensor appear, making its contribution dominant for the effective viscosity. After $t \sim 60$ orbits the Maxwell tensor grows again, most probably due to slow-growing MRI modes. Indeed density and magnetic waves (with smaller amplitude) are excited at the transition region, due to the energy injection from the active region.

5.2. Comparing Different Resistivity Setups

In order to understand the dependence of each quantity on the distance from the transition region, in Figure 7 we show the effective viscosity α as a function of x averaged in the $y = z$ plane for RESA (top), RESB (center), and RESC (bottom). The quantities are averaged over 20 orbital times, in the saturated state. It is clear that the turbulence is sustained through the transition region and in the resistive region in RESB and RESC even if the average value of α in the resistive region is less than

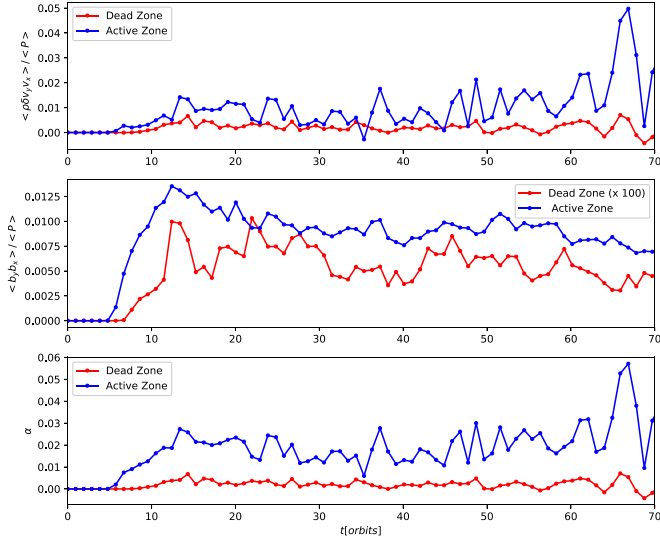


Figure 6. (Top) Reynolds tensor; (center) Maxwell tensor; (bottom) stress tensor for simulation RESB, normalized with the average pressure P at each time step.

20% of the value in the ideal zone for both cases. The 10 times higher resistivity value in simulation RESA produces a sharper transition in the magnetic turbulent activity, reflected in lower values of α . In all three setups the Reynolds tensor is highly fluctuating, keeping the effective viscosity α relatively high even in RESA. The sharper transition for RESC is slightly visible at $|x| = 2$ where the magnetic stress tensor falls from 5×10^{-3} to 0. The Reynolds, and thus the resulting total stress tensor, do not differ significantly in RESB and RESC because the feedback on the velocity due to the sharper resistivity transition occurs through the magnetic fluctuations, appearing quite smooth in both cases. From this analysis, it emerges the most important parameter to determine the turbulence behavior is the actual value of the resistivity in the dead zone, while the thickness of the transition region does not significantly affect the turbulence values.

5.3. Magnetic Dissipation

We checked the magnetic dissipation integrated over volume to better understand the resistive case stress tensor saturation level. We calculated $|\mathbf{J}|^2 = |\nabla \times \mathbf{B}|^2$, then we multiplied it by the numerical resistivity $\eta_N \sim 0.0002$; in the resistive cases we adopted the resistivity defined in Equation (10) plus the numerical resistivity value η_N . The results are plotted in Figure 7 (solid black line). We found the magnetic dissipation to be significantly stronger in the ideal region, and in general in ideal simulation IDB. This suggests the magnetic flux penetration in the dead zone occurs only in the layers closer to the active area and limits the possibility to dissipate magnetic field further inside the resistive region, eventually leading to plasma heating when the feedback on temperature is taken into account, reflected in changes in the ionization degree only in the transition region. In Figure 7 (top) we can see in simulation RESA for $|x| < 2$ the dissipation is indeed zero. In RESB, instead, the dissipation is zero only in $|x| < 0.5$, suggesting a deeper penetration of the turbulent magnetic field in the resistive region. In Figure 7 (bottom, solid black line), we show the dissipation for run RESC, where the transition in the dissipation is very sharp. Even if not resolved, it allows us to conclude that the turbulence penetration through the

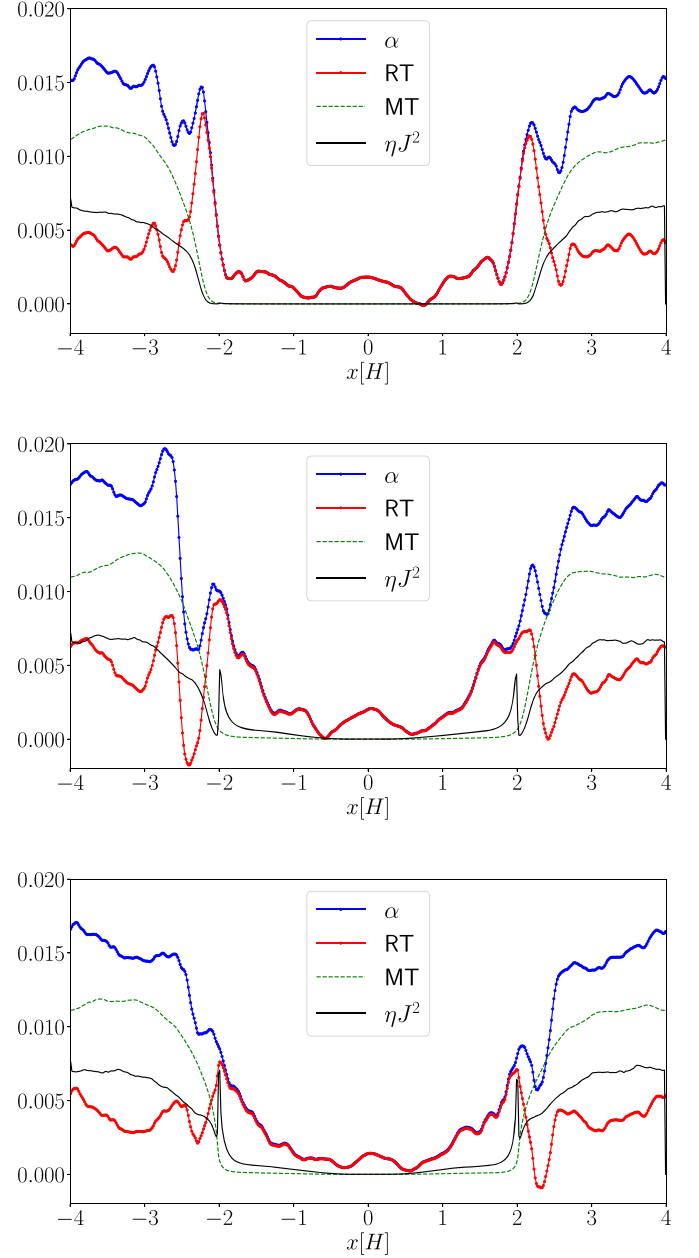


Figure 7. Effective viscosity $\alpha = \langle T_{xy}(t) / P(t) \rangle_{y,z,t}$ and breakdown in the hydrodynamical stresses $\langle R_{xy}(t) / P(t) \rangle_{y,z,t}$ and magnetic stresses $\langle M_{xy}(t) / P(t) \rangle_{y,z,t}$ for simulation RESA (top), RESB (center), and RESC (bottom), where $P(t)$ is the pressure at each point and time step and T_{xy} is defined in Equation (6). The spatial average is in the y - z plane and the average in time is over 20 orbits in the saturated phase (25–45 orbital times). The black solid line shows the magnetic dissipation $\eta|\mathbf{J}|^2$; see the text for further explanation.

boundary of the dead zone region is determined by the value of the resistivity itself, through the magnetic dissipation process.

5.4. Density Accumulation and Streams at the Transition from the Dead to the Active Zone

One of the characteristic features of the resistive setup is the presence of density peaks in the dead zone or, as appears after a more detailed analysis, in the proximity of the transition regions. In Figure 8 we show the variation of the profiles in the x direction as a function of time for simulation RESB. The density peak starts forming after around six orbits with MRI

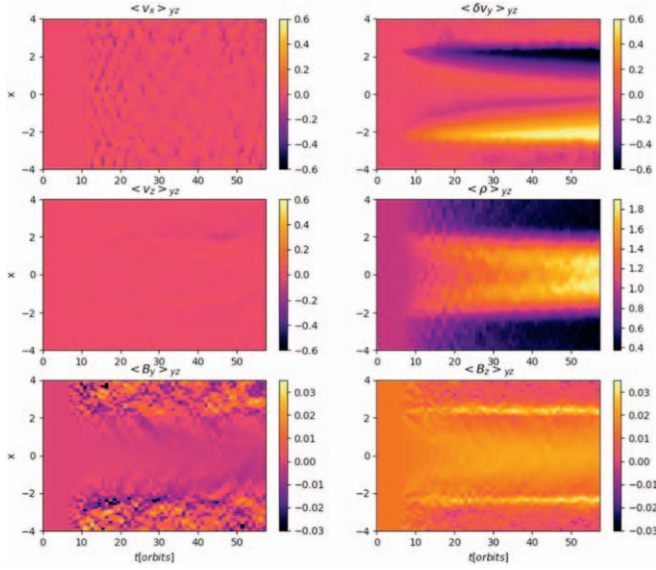


Figure 8. 2D profiles of the fields, averaged in the y, z directions for different x (vertical axis), as a function of time (horizontal axis), for simulation RESB. On the left column: (top) x and (center) z components of the velocity field; (bottom) y component of the magnetic field (generated by the MRI). The right column shows: (top) y component of the turbulent velocity $\delta v_y(t) = (v_y(t) - v_0)_{\max}$ and (center) density; (bottom) z component of the magnetic field. It is evident there is a temporal and spatial correspondence of the features characterizing the quantities in the right column, suggesting a common physical process originating them.

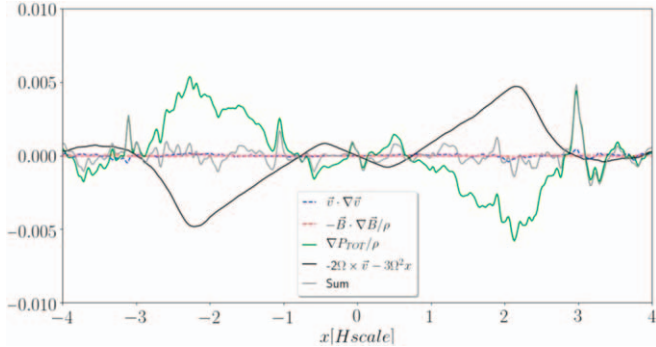


Figure 9. Momentum (Equation (1)) balance for RESB. The total pressure tensor (green solid line) balances the fictitious forces, i.e., Coriolis and centripetal force (black solid line). The other terms present small fluctuations. Each term is normalized to the maximum of the centrifugal force.

kicking in (see the corresponding stress tensors), in correspondence with the formation of an additional velocity component in the y direction at the transitions between the ideal and the dead zone. The density peak reaches $\rho = 1.6\rho_0$. In Figure 9 we show each contribution to the x component of Equation (2), where it is clear that the balance for the fluid pressure term comes from the Coriolis force. Since we employ an isothermal equation, the density has the same role as the pressure in the force balance, i.e., its profile is altered by the changing in the Coriolis force in the nonuniform resistivity setup of run RESB.

5.5. MRI Density Structures

The timescales for the formation of density and stream structure are very similar and in order to prove they are strictly connected with the MRI linear development (before saturation), we plot $\delta\rho_{\max}(t) = (\rho(t) - \rho_0)_{\max}/\rho_0$ and $\delta v_y(t)_{\max} = (v_y(t) - v_0)_{\max}/\text{MAX}(v_0)$ maximum values in x direction as a

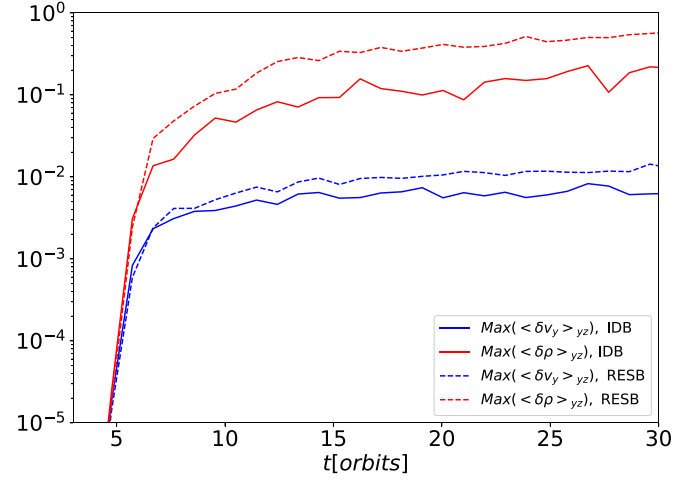


Figure 10. Density and y -component perturbation maximum values in the x direction, as a function of time, normalized with $\text{Max}(v_0)$ and $\text{Max}(\rho_0)$ respectively. The dashed lines correspond to simulation IDB while the solid lines correspond to simulation RESB.

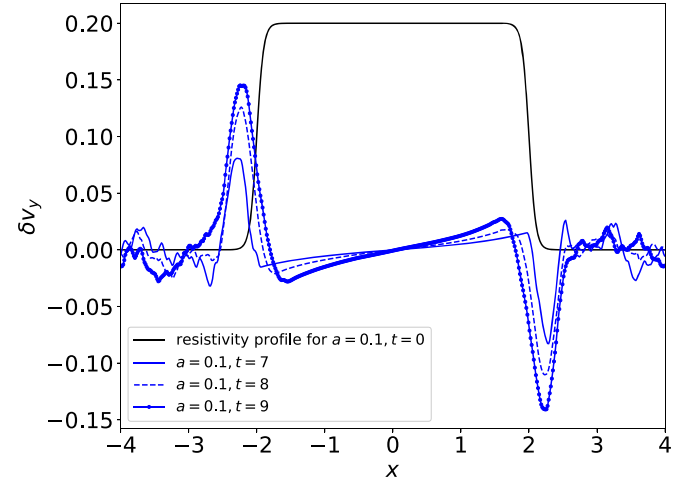


Figure 11. Resistivity and $\delta v_y = v_y - v_0$ as a function of the x coordinate for simulation RESB, when MRI is kicking in and the velocity fluctuations form: solid ($t = 7$ orbital times), dashed ($t = 8$ orbital times), solid and dotted ($t = 9$ orbital times). The peaks form in correspondence to the resistivity gradient.

function of time, both for IDB and RESB (Figure 10), where the subscript 0 indicates those are the initial values. The logarithmic scale on the vertical axis shows the growth rate of both the velocity and density perturbation is exponential and the saturation value is just slightly larger in the resistive case, supporting the idea that the resistivity gradient alters the MRI linear evolution. In Figure 11 we show δv_y profiles at different times for simulation RESB. The velocity fluctuations are about $\sim 30\%$ of the initial local shearing flow. The amplitude of these velocity perturbations, with respect to the background shear, is comparable to the peak velocity fluctuation amplitude in the center of the ideal part of the domain. As shown by Nauman & Blackman (2017), velocity structures can appear in the turbulent domain which, for sufficiently high Reynolds and magnetic Reynolds numbers, should contribute to form smaller turbulent structures. While this is a very interesting and important topic and deserves to be investigated further, in our simulation we can clearly see that the modification of the “local Keplerian flow” (in the

shearing box the rotation is approximated with a linear velocity profile) occurs in correspondence to the resistivity gradient. Similar analysis on RESC shows the steeper the transition for the resistivity profile, the more localized the velocity perturbations.

5.6. Comparison with Similar Findings in the Literature

This density peak has been observed in other simulations before, e.g., in Kato et al. (2009, 2010, 2012) and in Faure et al. (2014), even with a more realistic resistivity depending on the temperature profile. Even if the setups in these works are different, the density feature can be explained as the effect of the MRI itself developing in a setup with a nonuniform resistivity (Kato et al. 2009, 2010). Kato et al. (2010) noticed the angular velocity profile of gas is modified when MRI is excited nonuniformly in a part of a disk. By the end of the linear phase of the MRI, the velocity profile (in the shearing direction) exhibits a rigid rotation in correspondence to the transition between the active and inactive regions. Indeed we expect the MRI not to be active in the region where the macroscopic magnetic Reynolds number $R_m < 1$. In particular, following Fleming et al. (2000), these are the regions where $R_m \sim R_m^{\text{cr}}$. In our simulation RESB, as opposite to Kato et al. (2009), the modification to the initial velocity profile seems to accelerate the shearing velocity at the transition region. This is due to the fact that the net effect of the MRI is to redistribute angular momentum within the box: the MRI inactive layer, close to regions where the MRI is active, are dragged by the nearby active layer. Note that, while there is no actual angular momentum transport in a shearing box simulation, the angular momentum is redistributed by MRI over the box. If this active region is characterized by a higher speed than the local dead zone, the latter is sped up as in our case and, vice versa, the outer inactive layer is slowed down by the slower MRI active layer (Kato et al. 2010).

5.7. Density Accumulation as a Diffusion Process

Another way to understand the density enhancements is through a turbulent diffusion process linked to the turbulence strength $D \propto \alpha$ (see, e.g., Kalinske & Pien 1943), where the diffusion coefficient enters into the evolution of the density as

$$d\rho/dt \sim \nabla \cdot (D\nabla\rho). \quad (11)$$

In the x (radial) direction, Equation (11) becomes

$$d\rho/dt \sim (dD/dx)(d\rho/dx) + Dd^2\rho/dx^2.$$

The first term on the right-hand side can be interpreted as an advection equation with the advection velocity of $-dD/dx$. In the transition region, dD/dx is large because, as shown in Figure 7, α varies significantly across the transition region. As D is large in the active zone but small in the dead zone, this can produce a net mass flux from the former to the latter. Once the pressure and thus the density distribution is altered, the disk adjusts itself so that the pressure gradient is balanced by the Coriolis force, and the quasi-steady state is achieved.

5.8. Spectra in the Resistive Models

We investigate the spectral features in the shearing direction, considering averages as defined previously (see Equations (7)–(9)), i.e., fields averaged in z , and then spectra at different positions x_1 averaged over time ($t = 25$ –45 orbits). In Figure 12 (left), we can see the velocity spectra for RESB,

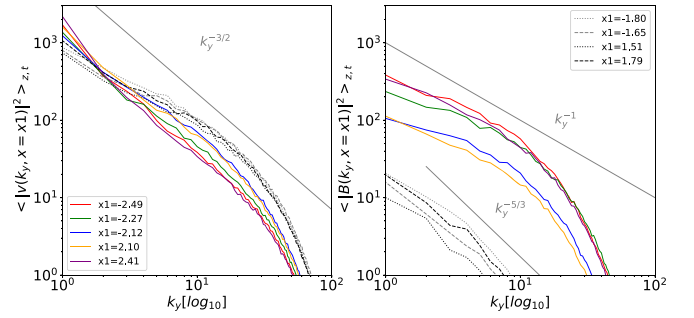


Figure 12. 1D spectra in the y direction for simulation RESB, averaged in the vertical direction and time (last 10 orbits). Different colors label the location in the x direction. Colors label the active layers, while black and gray dashed and dotted lines label the resistive layers. For a better visualization the legend is spread among the two panels and refers to both of them.

where colors label different values of x , i.e., specific distances from the boundaries between the dead and active zones. When compared to the previous kinetic energy spectra, we immediately notice a difference between the active and dead zones. As before, in the active regions, the spectra are compatible with a $-3/2$ slope. Velocity field fluctuations are present also in the dead zone, but the kinetic energy is strongly suppressed there at larger scales, while smaller-scale fluctuations appear to propagate into the dead zone, where the spectra become flatter. This must be due to the interplay of the inhomogeneously developing MRI instability and the propagation of density fluctuations. The rms of the magnetic field is plotted in Figure 12 (right). Compared to the ideal simulation IDB, the magnetic energy is strongly quenched in the dead zone. In the active region the spectra are flat. As before it is difficult to really identify a power law, but the scaling like k_y^{-1} for about one decade from the large injection scales is not far off. The dead layers are characterized by significantly lower magnetic energies (almost two orders of magnitude less), but there is a steeper slope, characterized by a Kolmogorov-type spectrum for about one decade. This suggests that the dynamics in the dead zone is not dominated directly by energy injection from the MRI, but rather a more complex process involving injection via the velocity field and density that penetrates the dead zone.

6. Conclusions

The main goal of our study was to quantify the turbulence and dynamics in the proximity of the radial transition region in the saturated phase of the MRI. In this work we performed shearing box simulations using the Athena++ code, with a nonuniform Ohmic resistivity in the radial direction. Our analysis shows that the most important parameter to determine the turbulence behavior is the actual value of the resistivity in the dead zone, while the thickness of the transition region does not significantly affect the turbulence values. In addition, from the computational point of view, this work confirms that resolving the transition region is not fundamental to determining the physics across the boundary itself, which supports the validity of results on the dynamics of the transition region in global domains, where small scales are not actually resolved. Global simulations are extremely expensive, being devoted to capturing matter accretion and the effect of winds, the latter being particularly relevant for transport in turbulence-inhibited regions. The resolution required to study the physics and the dynamics at this key region, especially for different plasma parameters, can only be achieved in local simulations.

6.1. Findings and Results

For comparison we performed “ideal” simulations, for which for our fiducial model is IDB. In these runs an actual resistivity is provided by a finite spatial grid. We observe a saturation of the viscous stress $\alpha \sim 0.035$. Our resistive models are characterized by a nonuniform explicit Ohmic resistivity in the radial direction. The radial profile of the resistivity transitions linearly from zero to η , defining two active zones, and a dead zone in the center of the simulation domain. Our fiducial model RESB shows a saturation phase (lasting about 30 orbits), during which the magnetic contribution is the most relevant for the stress tensor. The magnetic field dissipates quickly in the dead zone, but the velocity perturbation propagates beyond the transition region into the resistive area, sustaining turbulence with an effective α at the center of the resistive region of $\sim 20\%$ of the (average) ideal MHD region, both for run RESB and run RESC (the latter is characterized by a shorter, unresolved transition region for comparison). In simulation RESA, however, for which the explicit resistivity value η is 10 times larger than in RESB, the dead zone region is magnetically dead. For all the resistive simulations, the turbulence level in the active areas of the domain rises to $\sim 30\%$ of the ideal MHD region, up to one scale height deep into the resistive region (within $|x| = 1.5$ and $|x| = 2.5$ in Figure 7), depending on the explicit resistivity value. We observe a sharp transition in the Maxwell tensor from the MRI turbulent active areas to the dead zone. On the other hand, the sharper transition does not affect significantly the effective viscosity. The 1D Fourier spectra in the shearing direction can be fitted with a slope compatible with a $-3/2$ scaling; the magnetic field exhibits a flat spectrum at large scales, then falls off at values consistent with the estimated numerical dissipation scales. Energies at large scales are comparable for the velocity and magnetic field. In our resistive fiducial model (RESB) the velocity spectrum can again be fitted with a $k_y^{-3/2}$ slope in the active layers, while it flattens at large scales for the dead layers, resembling a k_y^{-1} slope. While in the active region the spectra are flat, scaling like k_y^{-1} for about one decade from the large injection scales, the dead layers are characterized by significantly lower energies, almost two orders of magnitude less than the ideal regions. In conclusion, the spectra do not reveal significant features in transition between the active and the dead zone, while the magnetic energy is clearly quenched at all scales in the resistive region and in the transition region.

6.2. Comparison with the Literature

In the “ideal” simulations we observe a saturation of the viscous stresses comparable with and in agreement with previous literature (see, e.g., Hawley et al. 1995), where a similar resolution is adopted in the vertical direction ($64/H$). The main contribution to the transport comes from the Maxwell tensor, as expected. We observe that the result on the “radial” transition to the dead zone, which retains some turbulent activity and fluctuations of the Reynolds stress, is similar to that found in Fleming & Stone (2003) for the vertically stratified shearing box, i.e., the vertical variation of the ionization degree while, in our case, the nonuniform resistivity takes into account the variation of the ionization degree in the radial direction. Global dynamics can change the thermal structure of the disks. For example, Faure et al. (2014), using a model where the dissipation in the system has feedback on the temperature profile and a simple

prescription for radiative cooling, pointed out the importance of heating caused by waves propagating adiabatically through the dead zone, and dissipating as weak shocks. This result is important when the heating is taken into account (thus for more realistic models); changing the temperature, these waves can also change the resistivity profile, and thus the location of the transition region. These global effects will be studied in future papers. Consistently with Kato et al. (2009), our resistive setups show the resistivity gradient alters the angular momentum redistribution at the boundaries between the active and dead zones. In the stationary phase the strong velocity gradient can be expressed in terms of the resistivity gradient, which is significantly high in the transition region. While this is not the primary explanation for density accumulation and planetesimal growth at the boundary of the dead/active zone, this might be a competing important effect.

6.3. Relevance and Limitations of This Work

As found by Nauman & Blackman (2017), the critical Reynolds numbers for which turbulence can be sustained in the active zones is still a matter of debate. High numerical resistivity might result in wrong consideration of the parameters determining the sustainability of MRI and its saturation values. This work is relevant in the context of PPDs, for which the role of non-ideal MHD effects has been recognized in the region $r > 1$ au, where dust grains are most probably trapped and evolve into planetesimals. An example is the work by Okuzumi & Ormel (2013) which presented simple scaling relations for the planetesimal stirring rate in turbulence-driven MRI, taking into account the stabilization effect of an Ohmic resistivity. These findings motivate an investigation of the chemistry and radiation processes required to provide the correct nonideal coefficients that are particularly relevant in affecting the turbulence dynamics; see, e.g., the recent paper by Gressel et al. (2020). The combined effect of radial transition/vertical stratification should also be taken into account to understand the transport and accretion in a realistic PPD model. In particular, vertical stratification may allow the formation of the so-called *zonal flows* (Johansen et al. 2009; Kunz & Lesur 2013; Bai & Stone 2014), contributing to create denser regions at different heights, balancing the momentum equation in the disk. As discussed in the introduction, the equatorial plane of the disk is also interesting with regard to nonideal effects other than Ohmic resistivity, and connected with the chemical and radiation processes occurring within the disk and in the central star (see, e.g., Okuzumi & Hirose 2011; Gressel et al. 2015; Xu & Bai 2016).

We would like to thank Kazunari Iwasaki for discussions and insights on accretion in astrophysical disks and simulations. F.P. would like to thank Marco Velli and Silvio Cerri for discussions on MHD turbulence and energy transfer. F.P. would also like to thank Neal Turner for illuminating discussions on the results of this manuscript. The simulations presented in this paper were performed on Perseus supercomputer in Princeton University (<https://researchcomputing.princeton.edu/systems-and-services/available-systems/perseus>). This research was supported in part by the National Science Foundation under grant No. NSF PHY-1748958. K.T. was supported by Japan Society for the Promotion of Science (JSPS) KAKENHI grant Numbers 16H05998, 16K13786, 17KK0091, 18H05440. K.T. also acknowledges support by MEXT as “Program for Promoting Researches on the Supercomputer Fugaku” (Toward a unified view of the universe: from large-scale structures to planets).

ORCID iDs

Fulvia Pucci  <https://orcid.org/0000-0003-4161-8512>
 Kengo Tomida  <https://orcid.org/0000-0001-8105-8113>
 James Stone  <https://orcid.org/0000-0001-5603-1832>
 Shinsuke Takasao  <https://orcid.org/0000-0003-3882-3945>
 Hantao Ji  <https://orcid.org/0000-0001-9600-9963>

References

- Armitage, P. J. 2011, *ARA&A*, 49, 195
 Bai, X.-N. 2014, *ApJ*, 791, 137
 Bai, X.-N., & Stone, J. M. 2013, *ApJ*, 769, 76
 Bai, X.-N., & Stone, J. M. . 2014, *ApJ*, 796, 31
 Balbus, S. A., & Hawley, J. F. 2003, in *Turbulence and Magnetic Fields in Astrophysics*, ed. E. Falgarone & T. Passot (Berlin: Springer), 329
 Balbus, S. A., & Terquem, C. 2001, *ApJ*, 552, 235
 Béthune, W., Lesur, G., & Ferreira, J. 2017, *A&A*, 600, A75
 Blaes, O. M. 1994, *ApJS*, 92, 643
 Blandford, R. D., & Payne, D. G. 1982, *MNRAS*, 199, 883
 Bruno, R., & Carbone, V. 2013, *LRSP*, 10, 2
 Desch, S. J. 2004, *ApJ*, 608, 509
 Desch, S. J., & Turner, N. J. 2015, *ApJ*, 811, 156
 Faure, J., Fromang, S., & Latter, H. 2014, in *IAU Symp. 299, Exploring the Formation and Evolution of Planetary Systems*, ed. M. Booth, B. C. Matthews, & J. R. Graham (Cambridge: Cambridge Univ. Press), 157
 Fleming, T., & Stone, J. M. 2003, *ApJ*, 585, 908
 Fleming, T. P., Stone, J. M., & Hawley, J. F. 2000, *ApJ*, 530, 464
 Gammie, C. F. 1996, *ApJ*, 457, 355
 Gressel, O., Ramsey, J. P., Brinch, C., et al. 2020, *ApJ*, 896, 126
 Gressel, O., Turner, N. J., Nelson, R. P., & McNally, C. P. 2015, *ApJ*, 801, 84
 Hawley, J. F., & Balbus, S. A. 1995, *PASP*, 12, 159
 Hawley, J. F., Gammie, C. F., & Balbus, S. A. 1995, *ApJ*, 440, 742
 Hawley, J. F., Gammie, C. F., & Balbus, S. A. 1996, *ApJ*, 464, 690
 Ilgner, M., & Nelson, R. P. 2006, *A&A*, 445, 205
 Johansen, A., Youdin, A., & Klahr, H. 2009, *ApJ*, 697, 1269
 Kalinske, A. A., & Pien, C. L. 1943, *TrAGU*, 24, 530
 Kato, M. T., Fujimoto, M., & Ida, S. 2010, *ApJ*, 714, 1155
 Kato, M. T., Fujimoto, M., & Ida, S. 2012, *ApJ*, 747, 11
 Kato, M. T., Nakamura, K., Tandokoro, R., Fujimoto, M., & Ida, S. 2009, *ApJ*, 691, 1697
 Kunz, M. W., & Balbus, S. A. 2004, *MNRAS*, 348, 355
 Kunz, M. W., & Lesur, G. 2013, *MNRAS*, 434, 2295
 Lesur, G., Kunz, M. W., & Fromang, S. 2014, *A&A*, 566, A56
 Nauman, F., & Blackman, E. G. 2017, *PhRvE*, 95, 033202
 Okuzumi, S., & Hirose, S. 2011, *ApJ*, 742, 65
 Okuzumi, S., & Ormel, C. W. 2013, *ApJ*, 771, 43
 Pessah, M. E., Chan, C.-k., & Psaltis, D. 2007, *ApJL*, 668, L51
 Sano, T., Inutsuka, S., Turner, N. J., & Stone, J. M. 2004, *PTHPS*, 155, 409
 Sano, T., Inutsuka, S.-I., & Miyama, S. M. 1998, *ApJ*, 506, 57
 Sano, T., Miyama, S. M., Umebayashi, T., & Nakano, T. 2000, *ApJ*, 543, 486
 Sano, T., & Stone, J. M. 2002a, *ApJ*, 570, 314
 Sano, T., & Stone, J. M. 2002b, *ApJ*, 577, 534
 Shi, J.-M., Stone, J. M., & Huang, C. X. 2016, *MNRAS*, 456, 2273
 Simon, J. B., Bai, X.-N., Armitage, P. J., Stone, J. M., & Beckwith, K. 2013, *ApJ*, 775, 73
 Simon, J. B., Bai, X.-N., Flaherty, K. M., & Hughes, A. M. 2018, *ApJ*, 865, 10
 Simon, J. B., Lesur, G., Kunz, M. W., & Armitage, P. J. 2015, *MNRAS*, 454, 1117
 Stone, J. M., & Gardiner, T. A. 2010, *ApJS*, 189, 142
 Stone, J. M., Tomida, K., White, C. J., & Felker, K. G. 2020, *ApJS*, 249, 4
 Suzuki, T. K., & Inutsuka, S.-i. 2009, *ApJL*, 691, L49
 Suzuki, T. K., & Inutsuka, S.-i. 2014, *ApJ*, 784, 121
 Suzuki, T. K., Muto, T., & Inutsuka, S.-i. 2010, *ApJ*, 718, 1289
 Turner, N. J., Fromang, S., Gammie, C., et al. 2014, in *Protostars and Planets VI*, ed. H. Beuther et al. (Tucson, AZ: Univ. Arizona Press), 411
 Urpin, V. A. 1984, *SvA*, 28, 50
 Wada, K., & Norman, C. A. 1999, *ApJL*, 516, L13
 Wada, K., & Norman, C. A. 2007, *ApJ*, 660, 276
 Wardle, M. 1999, *MNRAS*, 307, 849
 Wardle, M. . 2007, *Ap&SS*, 311, 35
 Wardle, M., & Salmeron, R. 2012, *MNRAS*, 422, 2737
 Xu, R., & Bai, X.-N. 2016, *ApJ*, 819, 68
 Zeldovich, Y. B. 1981, *RSPSA*, 374, 299